Reacting and non-reacting, three-dimensional shear layers with spanwise stretching

Jonathan L. Palafoutas and William A. Sirignano

View Online   Export Citation   CrossMark

ARTICLES YOU MAY BE INTERESTED IN

Physics of Fluids

Special Topic: Paint and Coating Physics

Submit Today!

AIP Publishing

34, 123602

Reacting and non-reacting, three-dimensional shear layers with spanwise stretching

Jonathan L. Palafoutas[1,a)] (iD) and William A. Sirignano[2] (iD)

AFFILIATIONS

[1]Program in Applied and Computational Mathematics, Princeton University, Princeton, New Jersey 08540, USA
[2]Department of Mechanical and Aerospace Engineering, University of California Irvine, Irvine, California 92697, USA

a)Author to whom correspondence should be addressed: jpalafou@princeton.edu

ABSTRACT

A three-dimensional, steady, laminar shear-layer flow spatially developing under a boundary-layer approximation with mixing, chemical reaction, and imposed normal strain is analyzed. The purpose of this study is to determine conditions by which certain stretched vortex layers appearing in turbulent combustion are the asymptotic result of a spatially developing shear flow with imposed compressive strain. The imposed strain creates a counterflow that stretches the vorticity in the spanwise direction. Equations are reduced to a two-dimensional form for three velocity components. The non-reactive and reactive cases of the two-dimensional form of the governing equations are solved numerically, with consideration of several parameter inputs, such as the Damköhler number, the Prandtl number, chemical composition, and free-stream velocity ratios. The analysis of the non-reactive case focuses on the mixing between hotter gaseous oxygen and cooler gaseous propane. The free-stream strain rate κ^* is predicted by ordinary differential equations based on the imposed spanwise pressure variation. One-step chemical kinetics are used to describe diffusion flames and multi-flame structures. The imposed normal strain rate has a significant effect on the width of downstream mixing layers as well as the burning rate. Asymptotically in the downstream direction, a constant width of the shear layer is obtained if the imposed normal strain rate is constant. The one-dimensional asymptotic result is an exact solution to the multicomponent Navier–Stokes equation for both reacting and non-reacting flows, although it was obtained using the boundary-layer approximation. A similar solution with the layer width growing with the square root of downstream distance is found when the imposed strain rate decreases as the reciprocal of downstream distance. The reduced-order asymptotic solutions can provide useful guidance in developing flamelet models for simulations of turbulent combustion.

Published under an exclusive license by AIP Publishing. https://doi.org/10.1063/5.0125269

I. INTRODUCTION

A. The role of vortex stretching in turbulent mixing and combustion

In order to study turbulent combustion in practical engines via computational analysis, it is necessary to establish sub-grid flamelet models that can be coupled with large-eddy simulations. The models must provide the burning rate based on the magnitudes of the strain rates and vorticity imposed by the larger turbulent flow. Since the flames are known to occur at smaller scales than the largest eddies in the flow, they often cannot be resolved by direct numerical simulation, thereby requiring a separate analysis. Fortunately, the flames typically occur on small scales where laminar behavior may be assumed. The purpose of this study is to give some foundation to recent three-dimensional flamelet models[1–3] based on vortex stretching. Specifically, those models assume an asymptotic form whereby the scalar variables and the three components of velocity vary with only one spatial variable.

Our aim here is to show whether and how a three-dimensional structure consisting of a shear layer with vortex stretching will asymptotically, with growing downstream distance, yield a dependence on only the transverse position across the shear layer. Both reacting and non-reacting cases will be examined.

A useful flamelet model must have a statistically accurate representation of the relative orientations on this smallest scale of the vorticity vector, scalar gradients, and the directions of the three principal axes for the strain rate. Several studies with direct numerical simulations (DNS) exist, which are helpful in understanding this important alignment issue for application to turbulent flows. Certainly for incompressible flow and generally for variable-density flow, one principal strain rate γ locally will be compressive, another principal strain rate α will be tensile, and the third can be either extensional or compressive and will have an intermediate strain rate β of lower magnitude than the other like strain rate. Specifically, $\alpha > \beta > \gamma$, $\alpha > 0$, $\gamma < 0$,

and, for incompressible flow, $\alpha + \beta + \gamma = 0$. Betchov[4] indicates that, for incompressible, homogeneous, isotropic turbulence, the case with $\beta > 0$ is most important for vorticity production and the turbulence energy cascade to smaller scales. Ashurst *et al.*[5] and Nomura and Elghobashi[6] show that the vorticity alignment with the intermediate strain direction is most probable in both cases of homogeneous sheared turbulence and isotropic turbulence, but especially in the case with shear. They find that the intermediate strain rate is most likely to be extensive (positive). Dresselhaus[7] predicts the tendency for alignment of the intermediate strain direction with the vorticity. Kerr[8] reports that large values of helicity are not found in the turbulence cascade process, thereby indicating that vorticity does not have strong alignment with the major compressive or major tensile strain direction.

Nomura and Elghobashi[9] find, for reacting turbulent flow, that in regions of heat release and variable density, alignment of the vorticity with the most tensile strain direction can occur. As the strain rates increase, the intermediate direction becomes more favored for vorticity alignment. The scalar gradient and the direction of the compressive strain are commonly aligned.[5,6,9–11] There is wide agreement that the most common intermittent vortex structures in regions of high strain rate are sheets or ribbons rather than tubes.

Based on those understandings concerning vector orientations, one may construct a flamelet model based on superposition of a strained counterflow and flow structure with vorticity. Such models have recently been created.[1–3] They are three-dimensional in the sense that three velocity components are determined, generally with some dependence on three spatial coordinates. However, the scalar variables in the counterflow configuration are dependent on one variable. Here, we attempt to provide support for the findings by showing that it can easily occur as the downstream asymptote for a shear layer subject to a compressive strain in the transverse direction. Following the guidance from the cited DNS studies, we choose a shear-layer configuration with the scalar gradient and the direction of the compressive normal strain aligned with each other and orthogonal to the vorticity vector. Any shear layer is also a vortex layer because vorticity is present in the sheet-like configuration. The imposed counterflow in our situation results in a stretched vortex layer.

As noted above, there is evidence from the DNS literature that these vortex layers or sheets can exist in both non-reacting and reacting turbulent flows. Further evidence is provided by stability analyses for incompressible flows. For non-reacting flows, Neu[12] works with the Burgers stretched vortex sheet, showing that it can be stable; however, for sufficient vortex strength (or insufficient imposed strain rate), it becomes unstable, causing formation of a periodic array of rolled-up concentrated vortices with stretched braids. Corcos and Sherman[13] address stability of a purely two-dimensional viscous vortex sheet without describing it as the Burgers stretched vortex sheet. The roll-up of the two-dimensional flow is examined. Corcos and Lin[14] study the stability under three-dimensional perturbations. Lin and Corcos[15] study the phenomenon further exploring streamwise vorticity. The general implication for turbulent combustion and the flamelet theory is that a vortical layer or sheet can exist. However, it can also become unstable through the roll-up mechanism leading to larger vortex-tube structures. This is consistent with the observation from DNS[5,6,9–11] and experiment[16] that both vortex layers and vortex tubes can exist in the same turbulent flow field.

This study relates to some interesting classical work on temporal, viscous vortex layers and vortex tubes subject to normal strain. A finding in those studies was that a balance between the diffusion and advection of vorticity could be achieved, resulting in a steady-state solution. Burgers,[17] followed by Rott,[18] examined the axisymmetric behavior of a stretched vortex tube for incompressible flow. The stretching (extensive or tensile strain) in the direction aligned with the vorticity vector resulted in an inward swirling motion. The steady-state solution of the axisymmetric Navier–Stokes equation (known as the Burgers stretched vortex tube) requires a matching of vorticity strength and viscosity such that radially outward diffusion of vorticity and radially inward advection of vorticity are in balance. The two-dimensional analog of the stretched vortex tube involves a viscous shear layer, which is simultaneously a vortex layer, subject to normal compressive strain in a direction orthogonal to the shear-layer stream direction and with the associated tensile strain aligned with the vortex vector. The solution of the steady-state configuration for this vortex layer has been attributed to the unpublished work presented in lectures by Burgers.[19] The two-dimensional analog is also mentioned without attribution by Batchelor,[20] where this layer is described as a vortex sheet. Neu[12] refers to this two-dimensional layer as the "stretched Burgers vortex sheet." Note that, in contrast, the description "vortex sheet" for an inviscid flow implies a mathematical discontinuity in velocity and a vortex sheet of zero thickness; see Saffman.[21]

The incompressible velocity field defined by the Burgers stretched vortex sheet has u_x, u_y, and u_z as the velocity components. The imposed normal strain rate S, kinematic viscosity ν, and free-stream velocity magnitude U are taken as positive constants. As $y \rightarrow \infty$, $u_x(x, y, z, t) \rightarrow U$, $\partial u_y / \partial y \rightarrow -S$, and $\partial u_z / \partial z \rightarrow S$; also, as $y \rightarrow -\infty$, $u_x(x, y, z, t) \rightarrow -U$, $\partial u_y / \partial y \rightarrow -S$, and $\partial u_z / \partial z \rightarrow S$. Then, the exact steady-state solution to the Navier–Stokes equations is found for the velocity components and the vorticity ω_z, whereby

$$u_x = U \operatorname{erf}\left(\sqrt{\frac{S}{2\nu}} y\right); \quad u_y = -Sy; \quad u_z = Sz,$$

and

$$\omega_z = -\frac{\partial u_x}{\partial y} = -U\sqrt{\frac{S}{2\pi\nu}} \exp\left(-\frac{Sy^2}{2\nu}\right).$$

Although the sheet is being stretched in the z-direction, diffusion of momentum and vorticity in the y-direction allows a balance with advection in the y-direction that results in a steady solution.

Our analysis considers a steady, spatially developing shear layer in the x-direction with a two-dimensional imposed strain in the yz-plane. The imposed strain can affect the growth of the shear-layer width with downstream distance. In principle, if the imposed strain rate is constant with x, an asymptote should be reached downstream, where the layer thickness becomes constant, which resembles the Burgers stretched vortex sheet. Variable density with a low Mach number will be considered. Both reacting and non-reacting flows will be studied.

B. Flamelet modeling

Laminar, two-dimensional shear layers with mixing of the fuel and the oxidizer and the resulting diffusion flames is a classical subject

of study (see Williams[22]). Two-dimensional planar and axisymmetric counterflow configurations of laminar diffusion flames have been studied extensively: Linán,[23] Peters,[24] Williams,[25] and Pierce and Moin.[26] More recently, Rajamanickam *et al.*[27] considered a three-dimensional flame configuration with both counterflow and a mixing layer, which resulted in a spanwise stretching; however, the use of a uniform Oseen velocity avoided the effects of shear and vorticity. In a series of papers, Sirignano[28–31] has considered three-dimensional flame configuration with shear, counterflow (and associated stretching), mixing, and combustion. Here, we extend the work of Sirignano[31] who considered similar and approximately similar solutions that reduced the order of the problem to one-dimensional equations. We will reduce the three-dimensional problem to a two-dimensional system of equations to consider spatial development of the layer.

Our formulation builds on some classical treatments of the shear layers and boundary layers with variable density. Crocco[32] studied the effects due to viscous heat generation for compressible flow over a two-dimensional flat plate. Howarth,[33] Illingworth,[34] and Stewartson[35] found compressible solutions by using a modification factor for incompressible solutions for a suite of related boundary layer problems.

Some time later, combustion scientists addressed counterflows where the fuel and the oxidizer streams oppose each other. Linán[23] found analytical solutions to such a counterflow problem using one-step Arrhenius chemistry. Bilger[36] used a more robust expression for chemical rate. Linán and Williams[37] extended the problem to account for temporal variation. There is uniform agreement that the presence of strain due to counterflow inhibits flame growth and temperature. Essentially, residence time can be considered as the reciprocal of the strain rate.

The recent study[31] addresses three-dimensional, steady laminar flow structures with mixing, chemical reaction, normal strain, and shear strain. The problem is reduced to a two-dimensional form. A one-dimensional similar solution is developed. This study reconsiders the non-reactive and reactive cases of the two-dimensional form of the governing equations. In particular, these equations are expressed as a stepwise algorithm to solve the two-dimensional flow numerically, which allows consideration of many different parameter cases related to the Prandtl number, chemical composition, and free-stream velocity ratios. The analysis here of the non-reactive case focuses on the mixing between gaseous oxygen at a temperature of 800 K and gaseous propane at $\frac{2}{3} \times 800 = 533$ K. The analysis of the reactive case considers both ambient streams to have a temperature of 300 K with an initial peak ignitor temperature of 2000 K. Both cases include an imposed normal strain and shear strain. Various Prandtl numbers, free-stream horizontal velocity ratios, and Damköhler numbers are considered.

In Sec. II, the analysis is presented. The results for three different configurations are presented in Sec. III, with conclusions following in Sec. IV.

II. ANALYSIS

The selection and development of steady-state equations that govern the flow, including the continuity, momentum, energy, and species continuity equations, are discussed in Subsection II A. Subsection II B offers a description of the finite-difference approximations and marching scheme utilized in this study. Subsection III C outlines this study's comparison with Sirignano's one-dimensional similar solution.[31]

A. Governing equations

We consider the governing equations with the boundary-layer approximation described by Sirignano[31] where the velocity component u, enthalpy h, and mass fraction Y_m are constant with the spanwise coordinate z. The free-stream flows are primarily in the x-direction with compressive normal strain in the y-direction and extensional normal strain in the z-direction, as depicted in Fig. 1. There is no imposed pressure gradient in the x-direction. Any pressure gradient in the y-direction caused by the imposed strain will not be consequential for the x-momentum equation. It follows that

$$\frac{\partial(\rho u)}{\partial x} + \frac{\partial(\rho v)}{\partial y} + \frac{\partial(\rho w)}{\partial z} = 0, \tag{1}$$

$$\rho\left(u\frac{\partial u}{\partial x} + v\frac{\partial u}{\partial y} + w\frac{\partial u}{\partial z}\right) = \frac{\partial}{\partial y}\left(\mu\frac{\partial u}{\partial y}\right), \tag{2}$$

$$\rho\left(u\frac{\partial w}{\partial x} + v\frac{\partial w}{\partial y} + w\frac{\partial w}{\partial z}\right) + \frac{\partial p}{\partial z} = \frac{\partial}{\partial y}\left(\mu\frac{\partial w}{\partial y}\right), \tag{3}$$

$$\rho\left(u\frac{\partial h}{\partial x} + v\frac{\partial h}{\partial y} + w\frac{\partial h}{\partial z}\right) = \frac{1}{Pr}\frac{\partial}{\partial y}\left(\mu\frac{\partial h}{\partial y}\right) - \rho Q\dot\omega_F, \tag{4}$$

$$\rho\left(u\frac{\partial Y_m}{\partial x} + v\frac{\partial Y_m}{\partial y} + w\frac{\partial Y_m}{\partial z}\right) = \frac{1}{Pr}\frac{\partial}{\partial y}\left(\mu\frac{\partial Y_m}{\partial y}\right) + \rho\dot\omega_m;$$

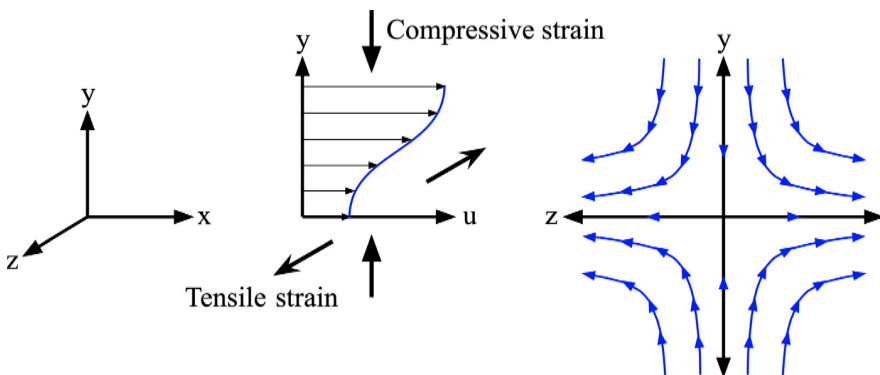$$m = \mathrm{O, F, CO_2, H_2O}, \tag{5}$$

FIG. 1. Schematic of shear mixing with imposed counterflow.

where O and F correspond to the oxidizer and the fuel. $\rho\dot\omega_F$ gives the mass consumption rate per unit volume.

The Prandtl number (Pr) is assumed to be constant and equal to the Schmidt number (Sc), which results in a unity Lewis number ($Le = Sc/Pr$). Radiation and gravity are not considered. At the low speeds considered, heat generation via viscous dissipation is neglected.

The compressive counterflow imposed in the y-direction causes a symmetry for pressure and an anti-symmetry for the w-component of velocity in the z-direction. w behaves according to the stagnation flow profile $w = \kappa z$, neglecting the terms of $O(z^2)$ in the yz-plane.[31] For the classical counterflow, no terms of $O(z^2)$ or higher will appear; thus, the description would be complete. Positive values of κ indicate that the flow field is stretched in the z-direction. To the same order, all other quantities are considered constant with z. We create a function

$$f(x) = \sqrt{-\left.\frac{\partial^2 p}{\partial z^2}\right|_{z=0}} > 0, \tag{6}$$

to describe the variation in pressure in z as a function of x. The square root of the second derivative is chosen because $\partial p/\partial z = 0$ on the $z = 0$ plane as a consequence of the spanwise symmetry for pressure. Under the boundary-layer approximation, pressure variation with y is neglected in the x-momentum equation. So, f is a function only of x. Therefore, the continuity equation (1) and the z-momentum equation (3) become

$$\frac{\partial(\rho u)}{\partial x} + \frac{\partial(\rho v)}{\partial y} + \rho\kappa = 0 \tag{7}$$

and

$$\rho\left(u\frac{\partial\kappa}{\partial x} + v\frac{\partial\kappa}{\partial y} + \kappa^2\right) - f(x)^2 = \frac{\partial}{\partial y}\left(\mu\frac{\partial\kappa}{\partial y}\right), \tag{8}$$

respectively. u, v, ρ, and κ vary with x and y, but not with z. Consistent with the boundary-layer theory, Eq. (7) will be considered to govern the velocity component v, while Eqs. (2), (4), (5), and (8) govern u, h, Y_m, and κ, respectively.

For the non-reactive case, $\dot\omega_F = \dot\omega_O = 0$. For the reactive case, a one-step chemical kinetics term appears in the energy and mass-fraction equations. One stream is composed of oxygen or a fuel-lean mixture, while the other stream is composed of propane or a fuel-rich mixture. $m = O$ corresponds to O_2, and $m = F$ corresponds to C_3H_8. The reaction rates of each gas are related by $\dot\omega_m = \dot\omega_F/\nu_m$, where ν_m is the stoichiometric ratio between propane and gas m by mass. ν is provided in Table I for each species. Q is the heating value of propane per unit mass.

We follow the Westbrook and Dryer[38] one-step reaction rate for propane

TABLE I. Chemical properties of all four species.

m	Molecular formula	$M\left(\frac{g}{mol}\right)$	$T_c(K)$	$V_c\left(\frac{cm^3}{g}\right)$	ν
O	O_2	32	154.55	2.5	0.275
F	C_3H_8	44	369.15	4.5	1.
	CO_2	44	304.15	2.1	0.334
	H_2O	18	647.14	5.2	0.612

$$\dot\omega_F = -A\rho^{0.75}Y_O^{1.65}Y_F^{0.10}e^{-E_a/R_F T_\infty h^*}, \tag{9}$$

where $A = 4.788 \times 10^8\,(kg/m^3)^{-0.75}/s$ is a reaction rate constant. The activation energy of propane in oxygen is $E_a = 30.0\,\frac{kcal}{mol}$, and the gas constant of propane is $R_F = 0.1885\,\frac{J}{g\,K}$. T_∞ and h^* will be defined hereinafter.

In order to make the results more general, the following normalized non-dimensional variables are created:

$$x^* = \frac{x}{x_0}; \quad u^* = \frac{u}{u_\infty}; \quad h^* = \frac{h}{h_\infty}; \quad \rho^* = \frac{\rho}{\rho_\infty},$$

$$y^* = \frac{y}{\delta_0}; \quad v^* = \frac{\sqrt{Re_0}}{u_\infty}v; \quad \kappa^* = \frac{x_0^2}{\delta_0 u_\infty}\kappa; \quad \mu^* = \frac{\mu}{\mu_\infty},$$

$$z^* = \frac{z}{\delta_0}; \quad w^* = \frac{\sqrt{Re_0}}{u_\infty}w; \quad f^*(x) = \frac{x_0 f(x)}{u_\infty\sqrt{\rho_\infty}}; \quad Q^* = \frac{Q}{h_\infty},$$

$$Da = \frac{Ax_0\rho_\infty^{0.75}}{u_\infty}; \quad Re_0 = \frac{\rho_\infty u_\infty x_0}{\mu_\infty}; \quad \delta_0 = \frac{x_0}{\sqrt{Re_0}}.$$

Upstream conditions are applied at $x = 0$. x_0 is the positive value used to normalize the x dimension. Based on the value of x_0, the Reynolds number is given as Re_0. δ_0 is an estimate of the boundary-layer thickness at $x = x_0$ and is used to scale the results for y and z. The subscripts ∞ and $-\infty$ are used to denote the free-stream behavior of a particular variable as $y \to \infty$ and $y \to -\infty$, respectively. A non-dimensional Damköhler number Da is created to define a normalized reaction rate of the fuel. This number offers a ratio between the chemical rate and the transport rate within the flow. This number will be large (of the order 10^6) because, in this study, chemical reactions occur much more rapidly than thermal or mass transport.

The governing non-dimensional equations become

$$\frac{\partial(\rho^* u^*)}{\partial x^*} + \frac{\partial(\rho^* v^*)}{\partial y^*} + \rho^*\kappa^* = 0, \tag{10}$$

$$\rho^*\left(u^*\frac{\partial u^*}{\partial x^*} + v^*\frac{\partial u^*}{\partial y^*}\right) = \frac{\partial}{\partial y^*}\left(\mu^*\frac{\partial u^*}{\partial y^*}\right), \tag{11}$$

$$\rho^*\left(u^*\frac{\partial\kappa^*}{\partial x^*} + v^*\frac{\partial\kappa^*}{\partial y^*} + \kappa^{*2}\right) - f^*(x^*)^2 = \frac{\partial}{\partial y^*}\left(\mu^*\frac{\partial\kappa^*}{\partial y^*}\right), \tag{12}$$

$$\rho^*\left(u^*\frac{\partial h^*}{\partial x^*} + v^*\frac{\partial h^*}{\partial y^*}\right) = \frac{1}{Pr}\frac{\partial}{\partial y^*}\left(\mu^*\frac{\partial h^*}{\partial y^*}\right) - \rho^* Q^*\dot\omega_F^*, \tag{13}$$

$$\rho^*\left(u^*\frac{\partial Y_m}{\partial x^*} + v^*\frac{\partial Y_m}{\partial y^*}\right) = \frac{1}{Pr}\frac{\partial}{\partial y^*}\left(\mu^*\frac{\partial Y_m}{\partial y^*}\right) + \rho^*\dot\omega_m^*;$$
$$m = O, F, CO_2, H_2O, \tag{14}$$

where

$$\dot\omega_F^* = -Da\rho^{*0.75}Y_O^{1.65}Y_F^{0.10}e^{-E_a/R_1 T_\infty h^*}. \tag{15}$$

Taking gaseous oxygen at 300K and 10bar where $\rho_\infty = 4.798\,\frac{kg}{m^3}$, $\mu_\infty = 42.43\,\frac{\mu Ns}{m^2}$, and $u_\infty = 1\,\frac{m}{s}$, we find $x_0 = 0.88mm$ for $Re_0 = 100$. The estimate of the thickness of the shear layer δ_0 under these conditions becomes $0.88/\sqrt{100} = 0.088$ mm. In the two-dimensional case with no imposed counterflow, the actual shear layer thickness at $x = x_0$ is found to be 0.39 mm, which is of the same order as our estimate; x_0 is approximately 2.3 times the shear-layer width that occurs at that x-position.

The specific heat at a constant pressure is taken to be constant throughout the domain and equal to $1309\,\frac{J}{kg\,K}$. This value is the average of the expected specific heat a at constant pressure of gaseous

oxygen ($988 \frac{J}{kg\,K}$) and gaseous propane ($1630 \frac{J}{kg\,K}$). Following the calorically perfect-gas assumption ($h = c_P T$)

$$T = T_\infty h^*. \tag{16}$$

Following the ideal-gas assumption and using a uniform-pressure assumption

$$\rho^* = \frac{T_\infty}{T} \frac{W}{W_O}; \quad W = \frac{1}{\sum\limits_{m=1}^{N} \frac{Y_m}{W_m}}. \tag{17}$$

μ is determined by taking the weighted average of the fluid viscosities

$$\mu = \sum_{m=1}^{N} Y_m \mu_m. \tag{18}$$

The viscosity of a particular fluid component at a given temperature $\mu_m(T)$ is found using the Chung et al.[39] relation for the viscosity of a dilute simple molecular gas, where

$$\mu_m(T) = \frac{(4.0785 \times 10^{-5}) T^{1/2}}{M_m^{1/6} V_{c,m}^{2/3} \left(\frac{A}{T^{*B}} + \frac{C}{\exp(DT^*)} + \frac{E}{\exp(FT^*)} + GT^{*B} \sin(ST^{*W} - H) \right)}. \tag{19}$$

M is the species molecular weight in $\frac{g}{mol}$, V_c is the critical volume in $\frac{cm^3}{g}$, and the dimensionless temperature T^* can be found as

$$T^* = 1.2593 \frac{T}{T_{c,n}}, \tag{20}$$

where T_c is the critical temperature in K. The empirical constants are given as $A = 1.161\,45$, $B = 0.148\,74$, $C = 0.524\,87$, $D = 0.773\,20$, $E = 2.161\,78$, $F = 2.437\,87$, $G = -6.435 \times 10^{-4}$, $H = 7.273\,71$, $S = 18.0323$, and $W = -0.768\,30$. This relation along with Eq. (19) determines μ at all points; μ^* is determined simply with its definition.

The molecular weight M, the critical temperature T_c, and the critical volume V_c of each fluid is summarized in Table I.

B. Computational scheme

The computational domain lies on the normalized x and y planes, where

$$x^* \in [0, L] \quad \text{and} \quad y^* \in [-H, H]. \tag{21}$$

L and $2H$ are the length of the computational domain in x^* and y^*, respectively. We choose $H > 1$ to ensure that the computational domain is wider in the y-direction than the mixing-layer thickness at $x = x_0$.

The domain is discretized into a rectilinear set containing N_x samples in x^* and N_y samples in y^* with the intention of developing stepwise algorithms to solve for quantities of interest downstream ($x^* > 0$). Finite-difference approximations of the differential terms are used, following Ferziger and Perić.[40]

First-order forward-difference approximations are substituted for the x-derivative terms and second-order central-difference approximations for the y-derivative terms. The y-derivative of a product of μ^* and another y-derivative is approximated to the second order with

$$\frac{\partial}{\partial y^*} \left(\mu^* \frac{\partial a}{\partial y^*} \right) \approx \frac{1}{\Delta y^{*2}} \left(\mu_{n+\frac{1}{2}}^{*k} a_{n+1}^k - \left(\mu_{n+\frac{1}{2}}^{*k} + \mu_{n-\frac{1}{2}}^{*k} \right) a_n^k + \mu_{n-\frac{1}{2}}^{*k} a_{n-1}^k \right), \tag{22}$$

where k and n are the indices for the x and y positions, respectively. $n \pm \frac{1}{2}$ denotes a half step between two grid points. μ^* is evaluated at half steps with

$$\mu_{n-\frac{1}{2}}^{*k} = \frac{\mu_{n-1}^{*k} + \mu_n^{*k}}{2} \quad \text{and} \quad \mu_{n+\frac{1}{2}}^{*k} = \frac{\mu_{n+1}^{*k} + \mu_n^{*k}}{2}. \tag{23}$$

Upstream and boundary conditions must be established for all quantities of interest in order for the solver to operate at the edges of the computational domain.

For u^*, κ^*, h^*, and Y_m in the non-reactive case, the initial upstream condition is a monotonic variation with y^* at $x^* = 0$. This study uses a hyperbolic tangent curve in these cases. For example, $u^*(0, y^*) = \frac{1}{2}\left(1 + \frac{u_{-\infty}}{u_\infty}\right) + \frac{1}{2}\left(1 - \frac{u_{-\infty}}{u_\infty}\right)\tanh(y^*)$. For h^* in the reactive case, an inflow with a temperature peak is given to allow ignition. In particular, a Gaussian curve is taken. We take $v^* = 0$ at $x^* = 0$ and $v^* = 0$ at $y^* = 0$.

The free-stream boundary conditions for u^*, κ^*, h^*, and Y_m are constant values. Later, κ_∞ and $\kappa_{-\infty}$ will be considered as functions of x.

Figure 2 illustrates mesh-size independence for the reactive case. Error is calculated using both sets of values of $\dot{\omega}_F^*$ from either mesh size. For the curves shown in Fig. 2, the maximum relative error is
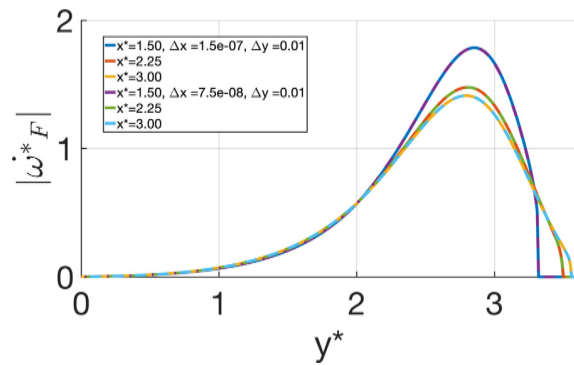

FIG. 2. $|\dot{\omega}_F^*(y^*)|$ at multiple positions in x^* for different mesh sizes in the case where reactions occur in the mixing layer.

6.7% when the error is normalized by the local values of $|\dot{\omega}_F^*|$ and 0.53% when the error is normalized by the maximum value of $|\dot{\omega}_F^*|$ at a particular value of x^*. $\dot{\omega}_F^*$ is used to test a numerical error because it is the most sensitive to changes in other parameters, thus ensuring mesh-size independence for all other parameters.

N_x and N_y cannot be chosen arbitrarily. The stability of our finite-difference scheme depends on the relationship between Δx and Δy, which can be recovered from the two-dimensional Navier–Stokes equations with negligible convection.[40] The criterion for stable computational results is given as follows:

$$\frac{\Delta x^*}{u^*} < \frac{1}{2}\frac{\rho^*}{\mu^*}\Delta y^{*2}. \tag{24}$$

In order to ensure that the changes due to the reaction rate do not happen more rapidly than the changes due to flow advection, the reaction rate of the fuel $\dot{\omega}_F^*$ must satisfy the following relation:

$$|\dot{\omega}_F^*| < \frac{u^*}{\Delta x^*}. \tag{25}$$

A stability condition is chosen which is stronger than necessary

$$|\dot{\omega}_F^*| < \frac{2\mu^*}{\rho^*}\frac{1}{\Delta y^{*2}} < \frac{u^*}{\Delta x^*}. \tag{26}$$

C. Comparing to the similar solution

Sirignano[31] devised a similar solution for the non-reactive case where κ is allowed to vary as $1/x$ in the free streams. Consequently, a function $G(x)$ will remain constant in each of the free streams where

$$G = \frac{2\kappa x}{u_\infty} = 2\kappa^* x^*. \tag{27}$$

Let us consider the ODEs that describe κ in the free streams. They result from setting the y-derivatives to zero in Eq. (8).

For $y^* \to +\infty$,

$$\frac{\partial \kappa_\infty^*}{\partial x^*} + \kappa_\infty^{*2} - f^*(x^*)^2 = 0, \tag{28}$$

where $\rho_\infty^* = u_\infty^* = 1$.

For $y^* \to -\infty$,

$$\rho_{-\infty}^* u_{-\infty}^* \frac{\partial \kappa_{-\infty}^*}{\partial x^*} + \rho_{-\infty}^* \kappa_{-\infty}^{*2} - f^*(x^*)^2 = 0. \tag{29}$$

With $\rho_{-\infty}^* = \frac{1}{\rho_\infty/\rho_{-\infty}}$ and $u_{-\infty}^* = \frac{1}{u_\infty/u_{-\infty}}$, the last ODE becomes

$$\frac{\partial \kappa_{-\infty}^*}{\partial x^*} + \frac{u_\infty}{u_{-\infty}}\kappa_{-\infty}^{*2} - \frac{u_\infty}{u_{-\infty}}\frac{\rho_\infty}{\rho_{-\infty}}f^*(x^*)^2 = 0. \tag{30}$$

Suppose f^* varies as

$$f^*(x^*) = \frac{F}{x^*}, \tag{31}$$

where F is some given positive constant. Thus, κ^* varies in the free streams as

$$\kappa_\infty^* = \frac{A_\infty}{x^*}, \tag{32}$$

and

$$\kappa_{-\infty}^* = \frac{A_{-\infty}}{x^*}, \tag{33}$$

which is the desired similar form of κ. This free-stream behavior in κ can be created after substitution of relations (31), (32), and (33) into (28) and (29). The A coefficients are determined by the solution of quadratic equations

$$A_\infty = \frac{1 \pm \sqrt{1+4F^2}}{2}, \tag{34}$$

and

$$A_{-\infty} = \frac{\dfrac{1}{u_\infty/u_{-\infty}} \pm \sqrt{\left(\dfrac{1}{u_\infty/u_{-\infty}}\right)^2 + 4\left(\dfrac{\rho_\infty}{\rho_{-\infty}}\right)F^2}}{2}. \tag{35}$$

Four combinations of the solutions for A_∞ and $A_{-\infty}$ become possible. Here, only the cases where both coefficients have the same sign will be considered, leaving two solutions. The positive (negative) values give a compressive (extensional) strain in the y-direction and an extensional (compressive) strain in the z-direction.

Note that here we differ from Sirignano,[31] who set

$$\kappa_\infty^* = \sqrt{\rho_{-\infty}^*}\kappa_{-\infty}^* = f^*(x^*), \tag{36}$$

which becomes approximately correct only if $F \gg 1$.

In a different case, where κ^* does not change along x in the free streams ($f^* = C$),

$$f^* = \kappa_\infty^* = C, \tag{37}$$

and

$$\kappa_{-\infty}^* = \sqrt{\frac{\rho_\infty}{\rho_{-\infty}}}C. \tag{38}$$

Three cases are investigated: κ_∞ ($\kappa_{-\infty}$) that is constant, κ_∞ ($\kappa_{-\infty}$) that varies as a positive constant divided by x^*, and κ_∞ ($\kappa_{-\infty}$) that varies as a negative constant divided by x^*.

We define a position variable η to demonstrate far downstream similarity. Following Sirignano[31]

$$\bar{y}(x,y) = \int_0^y \rho(x,y')dy'. \tag{39}$$

and

$$\eta(x,y) = \frac{\bar{y}(x,y)}{\sqrt{\dfrac{2\rho_\infty\mu_\infty x}{u_\infty}}}. \tag{40}$$

TABLE II. Parameter definitions for the non-reactive cases.

Case	f^*	$u_\infty/u_{-\infty}$	Pr	κ_∞^*
1	1	4	1.	1
2a	0	4	1.	0
2b	2	4	1.	2
3a	1	2	1.	1
3b	1	8	1.	1
4a	1	4	0.7	1
4b	1	4	1.3	1
5a	$1/x^*$	4	1.	$1.6180/x^*$
5b	$-1/x^*$	4	1.	$-0.6180/x^*$

TABLE III. Parameter definitions for the reactive cases.

Case	f^*	$u_\infty/u_{-\infty}$	Pr	Da
6	1	4	1.	1 500 000
7a	0	4	1.	1 500 000
7b	2	4	1.	1 500 000
8a	1	2	1.	1 500 000
8b	1	8	1.	1 500 000
9a	1	4	0.7	1 500 000
9b	1	4	1.3	1 500 000
10a	1	4	1.	0
10b	1	4	1.	750 000
11a	0	0.25	1.	1 500 000
11b	1	0.25	1.	1 500 000
11c	2	0.25	1.	1 500 000
12	1	4	1.	3 000 000

Substituting our definitions for normalized variables gives

$$\eta(x^*, y^*) = \frac{\int_0^{y^*} \rho^*(x^*, y')dy'}{\sqrt{2x^*}}. \tag{41}$$

III. RESULTS

The visualizations of the non-reactive flow when κ^* is held constant in the free streams are discussed in Subsection III A. Subsection III B discusses the non-reactive case, where κ^* varies with x^* in the free streams. Subsections III C and III D discuss the results of the reactive case, including an investigation of the multi-flame structures.

Table II summarizes the non-reactive flow cases, in which $h_\infty^* = 1$, $h_{-\infty}^* = 2/3$, $T_\infty = 800$ K, and $Da = 0$. κ_∞^* and $\kappa_{-\infty}^*$ in cases 5a and 5b are found according to Eqs. (32)–(35), where we consider only same-sign solutions for κ^* in the free streams.

Table III summarizes the reactive flow cases, in which $h_\infty^* = 1$, $h_{-\infty}^* = 1$, $h_{peak}/h_\infty = 20/3$, and $T_\infty = 300$ K. h_{peak}
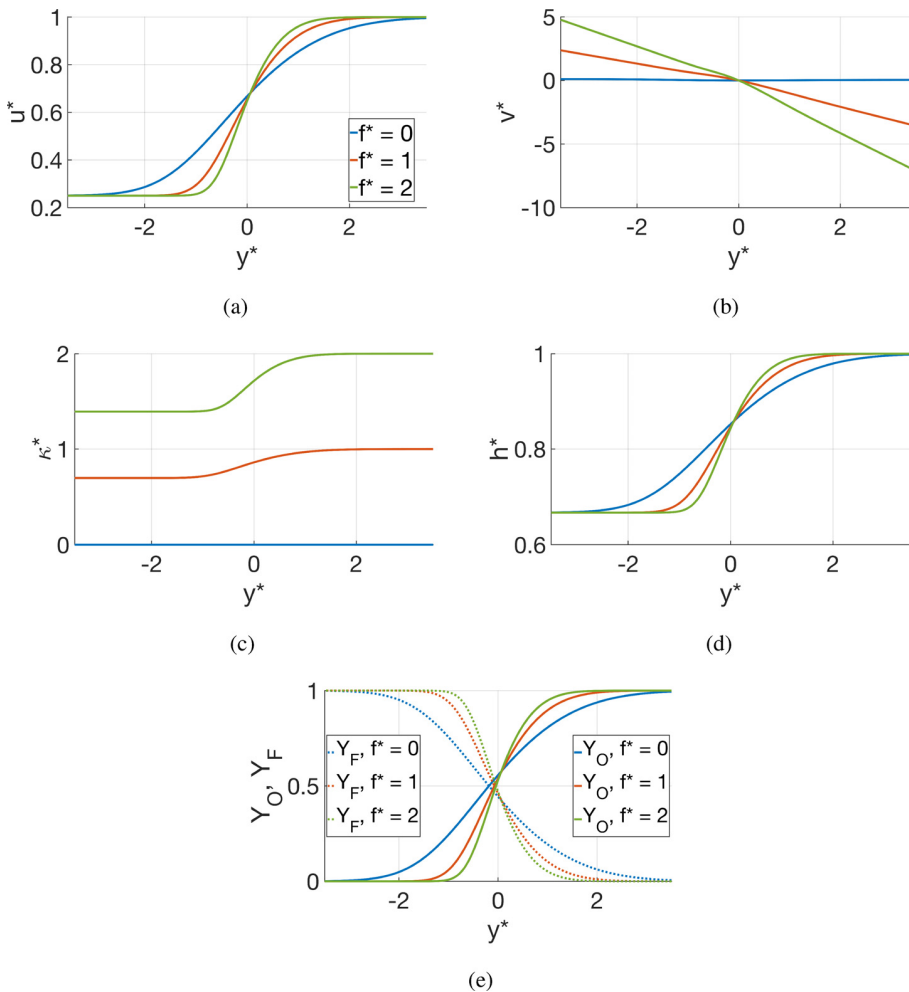

(a)

(b)

(c)

(d)

(e)

FIG. 3. u^*, v^*, h^*, κ^*, Y_O, and Y_F at $x^* = 1$ for non-reactive cases 2a, 1, and 2b. The ambient counterflow strain rate is constant with x^* and varies between 0 and 2. (a) $u^*(y^*)$, (b) $v^*(y^*)$, (c) $\kappa^*(y^*)$, (d) $h^*(y^*)$, and (e) $Y_O(y^*)$, $Y_F(y^*)$.
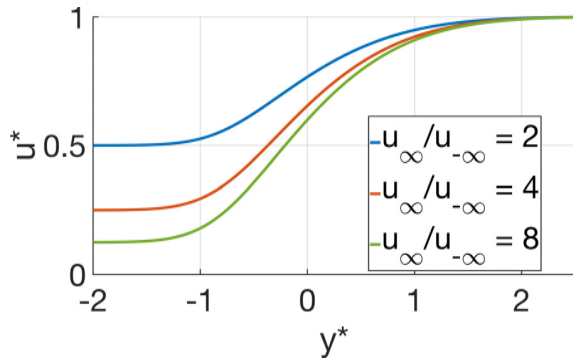
FIG. 4. u^* at $x^* = 1$ for non-reactive cases 3a, 1, and 3b. The free-stream velocity ratio varies from 2 to 8. The ambient counterflow strain rate is constant with x^*.

denotes the peak enthalpy of the ignitor at $x^* = 0$ and $y^* = 0$. κ^*_{∞} and $\kappa^*_{-\infty}$ are found according to Eqs. (37) and (38), respectively.

The boundary conditions $u^*_{\infty} = 1$ and $u^*_{-\infty} = u_{-\infty}/u_{\infty}$ are used for all cases. For the single-flame cases, we use $Y_{O,\infty} = 1$,

$Y_{O,-\infty} = 0$, $Y_{F,\infty} = 0$, $Y_{F,-\infty} = 1$, and $Y_{m,\pm\infty} = 0$ for $m = CO_2$, H_2O as the boundary conditions and explore the variations in these values for the multi-flame case.

A. Non-reactive layer with constant κ_{∞} and $\kappa_{-\infty}$

Figure 3 compares the effects of the two-dimensional flow ($f^* = 0$ with only two velocity components) to the three-dimensional flow ($f^* \neq 0$ with three velocity components). Figures 3(a), 3(d), and 3(e) show that increasing the flux and the strain rate of the counterflow, through an increasing f^*, decreases the width of the mixing layer for the scalar quantities. Thereby, the gradients and the vorticity are increased. Figure 3(b) shows that this effect also increases the inward velocity of the flow in the y-direction. In Fig. 3(c), we see the increasing value of the strain rate κ^* as a result of increasing f^*. As f^* increases, the flow field is stretched more strongly in the z-direction. Accordingly, the vortex stretching is greater since the same integral of vorticity occurs in a thinner layer. For all values of the constant f^*, an asymptote is reached downstream where the layer width becomes a constant, essentially making y to be a similarity variable for that asymptote.
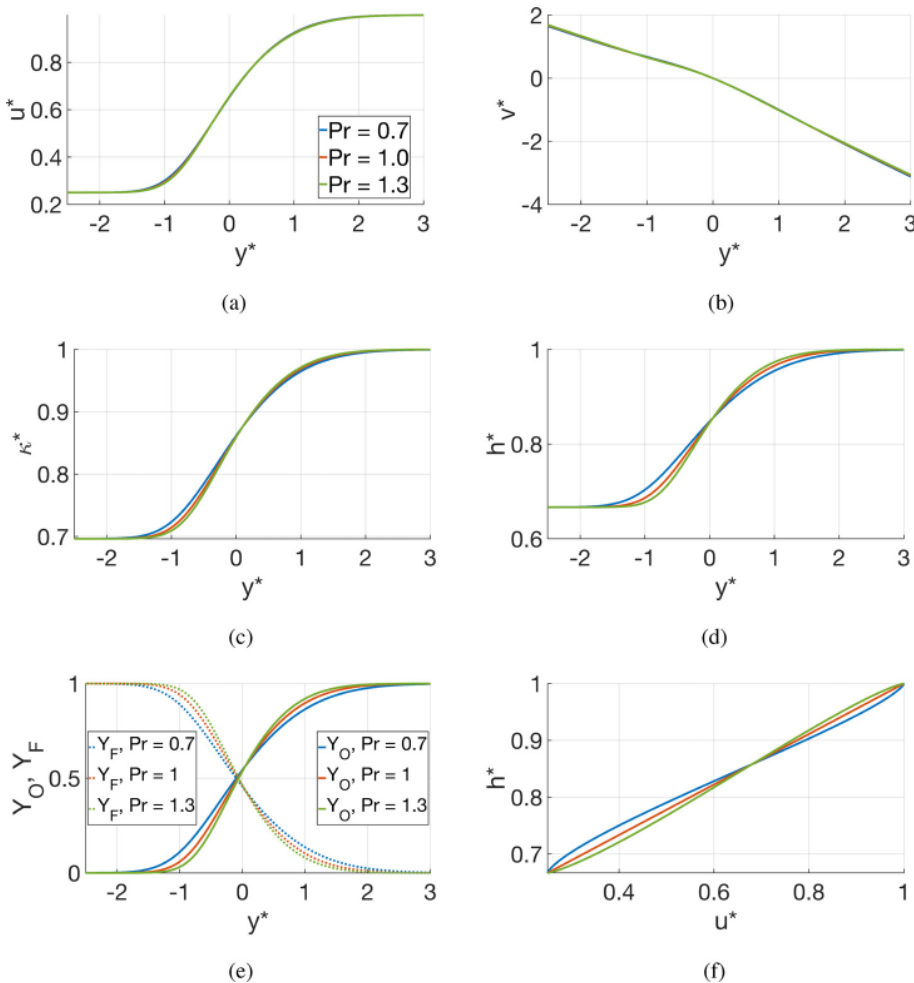

FIG. 5. u^*, v^*, h^*, κ^*, Y_O, and Y_F at $x^* = 1$ for non-reactive cases 4a, 1, and 4b. The Prandtl number varies from 0.7 to 1.3. The ambient counterflow strain rate is constant with x^*. (a) $u^*(y^*)$, (b) $v^*(y^*)$, (c) $\kappa^*(y^*)$, (d) $h^*(y^*)$, (e) $Y_O(y^*)$, $Y_F(y^*)$, and (f) h/h_{∞} as a function of u/u_{∞}.

Only u^* is shown in Fig. 4 because the ratio of the free-stream x-component velocities has a very minor effect on the downstream behavior of the other scalar quantities (v^*, κ^*, h^*, Y_O, Y_F) when all else is held constant. The use of u_∞ in the normalization results in a similarity of the behavior for many variables. The layer width is not affected by the velocity ratio; thus, the u-velocity gradient and the vorticity increase as the velocity ratio increases. However, the scalar gradients and the normal strain rates in the y- and z-directions are not affected significantly.

Figures 5(c)–5(e) reveal that as Pr increases, the mixing layers for the scalar quantities become thinner since thermal conductivity and mass diffusivity decrease, and large scalar gradients are regained. Figure 5(f) shows that a unitary Pr results in a linear relationship between the normalized enthalpy and the
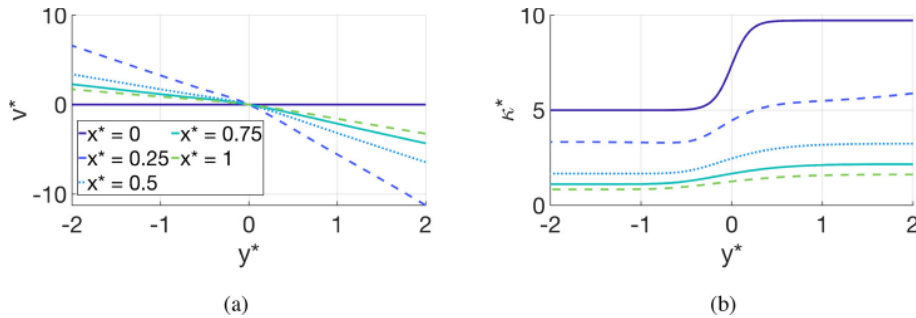

FIG. 6. Results for non-reactive case 5a at $x^* = 1$ with the positive value of $A_{-\infty}$. (a) $v^*(y^*)$ and (b) $\kappa^*(y^*)$.
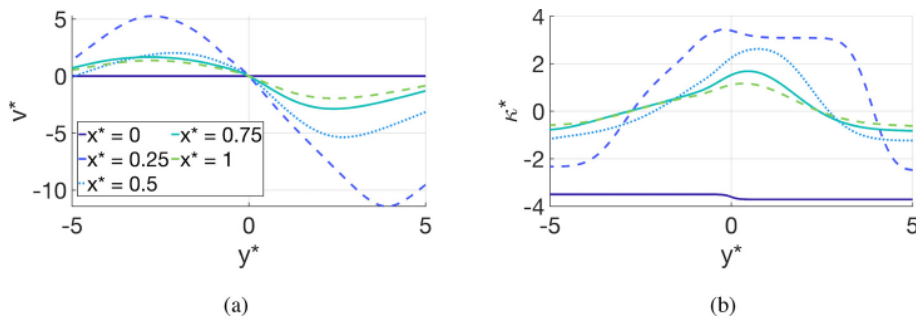

FIG. 7. Results for non-reactive case 5b at $x^* = 1$ with the negative value of $A_{-\infty}$. (a) $v^*(y^*)$ and (b) $\kappa^*(y^*)$.
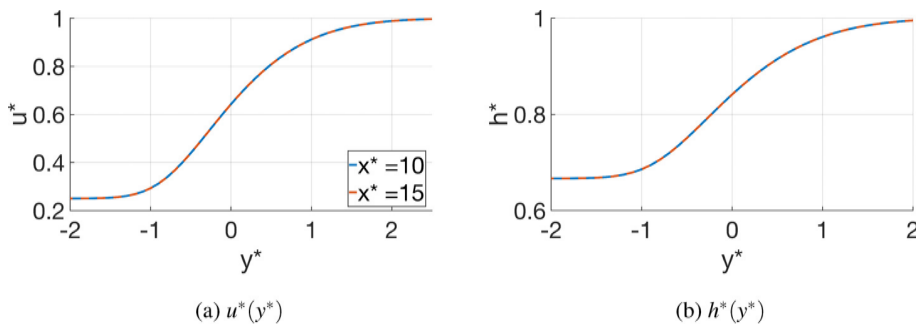

FIG. 8. Downstream similarity for u^* and h^* for the non-reactive case. Subfigures (a) and (b) are of case 1 where the imposed normal strain is constant with x^*. Subfigures (c) and (d) are of case 5a where the imposed normal strain varies as $1/x^*$.

normalized horizontal free-stream velocity; i.e., a Crocco integral forms.

B. Non-reactive layer with κ_∞ and $\kappa_{-\infty}$ as a function of x^*

Now, we solve the case where the strain rate κ^* is allowed to vary as $1/x^*$. The analytical solution for A_∞ and $A_{-\infty}$ yielded two solutions (one positive pair and one negative pair); thus, here, both cases are examined. In the case where the constants are positive, there is inflow with a compressive normal strain rate in the y-direction and outflow with an extensional normal strain rate in the z-direction. For this case, Fig. 6(a) shows that the inward y-velocity decreases with x^*. As the imposed compressive strain decreases with x^*, so will the rate of inflow in the mixing layer. Figure 6(b) shows the $1/x^*$ behavior of κ^* in the free streams. Clearly, the counterflow strength and its influence decreases here with increasing downstream distance.

In Fig. 7(b), for the case with the negative sign, the outer flow has inflow with a compressive normal strain rate in the z-direction and outflow with an extensional normal strain rate in the y-direction. However, reversal occurs in the interior mixing region. κ^* is negative

in the free streams and positive in the mixing regions, implying that there is inflow in the z-direction in the free streams and outflow in the z-direction in the mixing region. Nonetheless, the $-1/x^*$ behavior of κ^* is clear in the free streams of Fig. 7(b). Figure 7(a) shows the flow slowing in the y-direction in the free streams because the magnitude of the imposed extensive strain is decreasing with x^*.

In comparing the results for the two cases with different signs for the constants, it appears that a tendency toward vortex stretching occurs even when the outer flow (with the negative constant) would favor vortex shrinking or compression. One might question the stability of the case with the negative constant. Stability analysis is left for a future task.

Let us compare the behaviors far downstream for the cases from the prior subsection and this subsection. Figures 8(a) and 8(b) show downstream similarity for u^* and h^* with regard to y^*. With an imposed normal strain that is constant along the stream, the shear layer's growth is stopped, and the need for a new similarity coordinate is eliminated because y^* becomes the similarity variable downstream. Thus, it is clear that, asymptotically with increasing downstream distance, the shear-layer width becomes constant and a quasi-one-dimensional flow results, although three components of velocity are
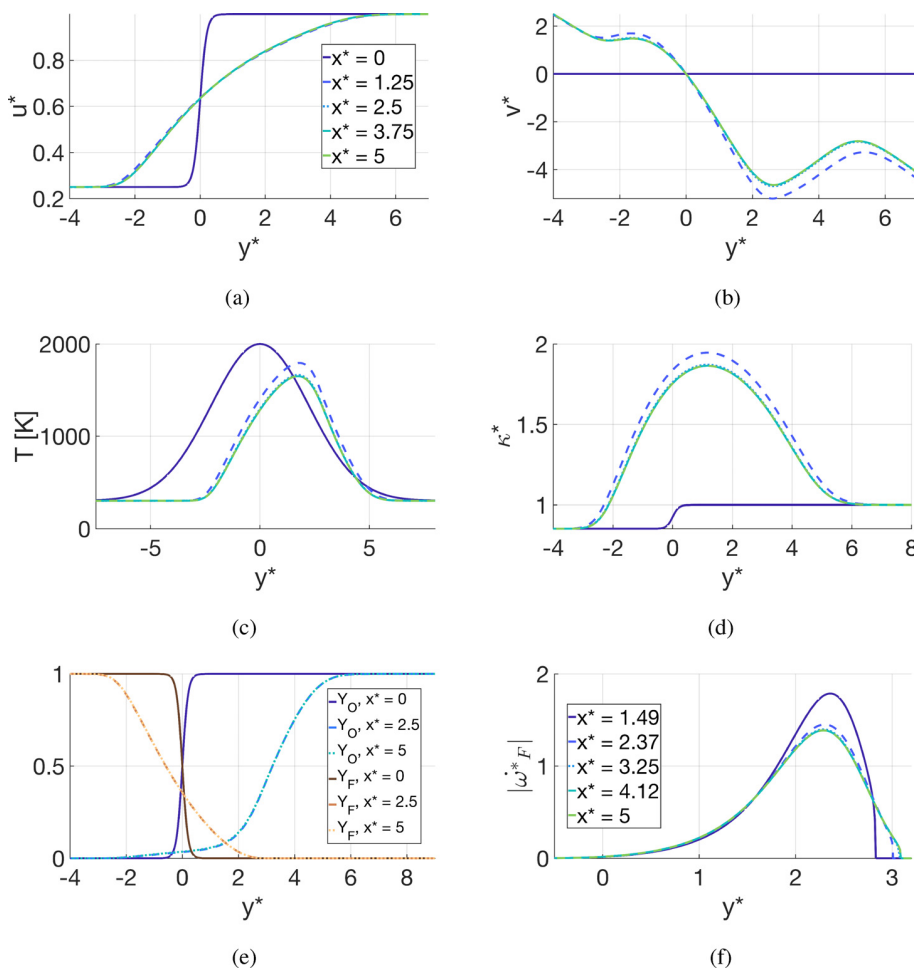

FIG. 9. Results for reactive case 6 from $x^* = 0$ to $x^* = 5$, where $f^* = 1$. (a) $u^*(y^*)$, (b) $v^*(y^*)$, (c) $T(y^*)$, (d) $\kappa^*(y^*)$, (e) $Y_O(y^*)$, $Y_F(y^*)$, and (f) $|\dot{\omega}_F^*(y^*)|$.

involved. In the incompressible limit, that asymptote for the non-reactive case is exactly the Burgers stretched vortex sheet.

A different observation is shown in Figs. 8(c) and 8(d) for the case where the imposed normal strain rate varies as the reciprocal of downstream distance; the shear-layer width grows approximately with $\sqrt{x^*}$, allowing a similarity coordinate, η, as seen in the classical shear layer theory.

C. Mixing Layer with a Diffusion Flame

Here, we consider pure propane fuel in the free stream at $y = -\infty$ and pure oxygen in the free stream at $y = \infty$. Upstream, a region of high temperature is provided in the layer. Therefore, we expect mixing of the two reactants in the shear layer, ignition, and establishment of a diffusion flame.

Figure 9 depicts the base reactive case (case 6) at several stations in x^* from 0 to 5. The results show that, if the imposed strain is constant with x^*, the reacting shear layer asymptotically reaches a constant width with increasing x^*. Thus, for both reacting and non-reacting cases with constant f^*, the asymptote becomes a similar

solution with y^* as the similarity variable. Furthermore, since x-derivatives disappear, the solution is exact for the multicomponent Navier–Stokes equation, albeit that they were obtained as asymptotes using the boundary-layer approximation. Here, we see an analogy with the Burgers stretched vortex sheet with the resulting asymptotic quasi-one-dimensional flow and albeit that three velocity components exist.

Figure 9(c) shows a converging temperature decrease with increasing downstream distance. The flame moves in the positive y-direction, toward the oxygen-rich, higher-speed stream. This temperature peak causes a local decrease in density, which increases the outflow velocity in the z-direction, as seen in Fig. 9(d). That is, the flow experiences a greater extensional strain in the z-direction near the flame. Where the density has decreased, the increased w^*-component of velocity maintains the imposed counterflow mass flux. Note that there is no increase in the mass flux in the x-direction. The y-velocity above and below this region is locally increased near the reaction zone in order to maintain the mass flux at a lower density value, as seen in Fig. 9(b). Figure 9(f) shows that the reaction rate of the fuel decreases
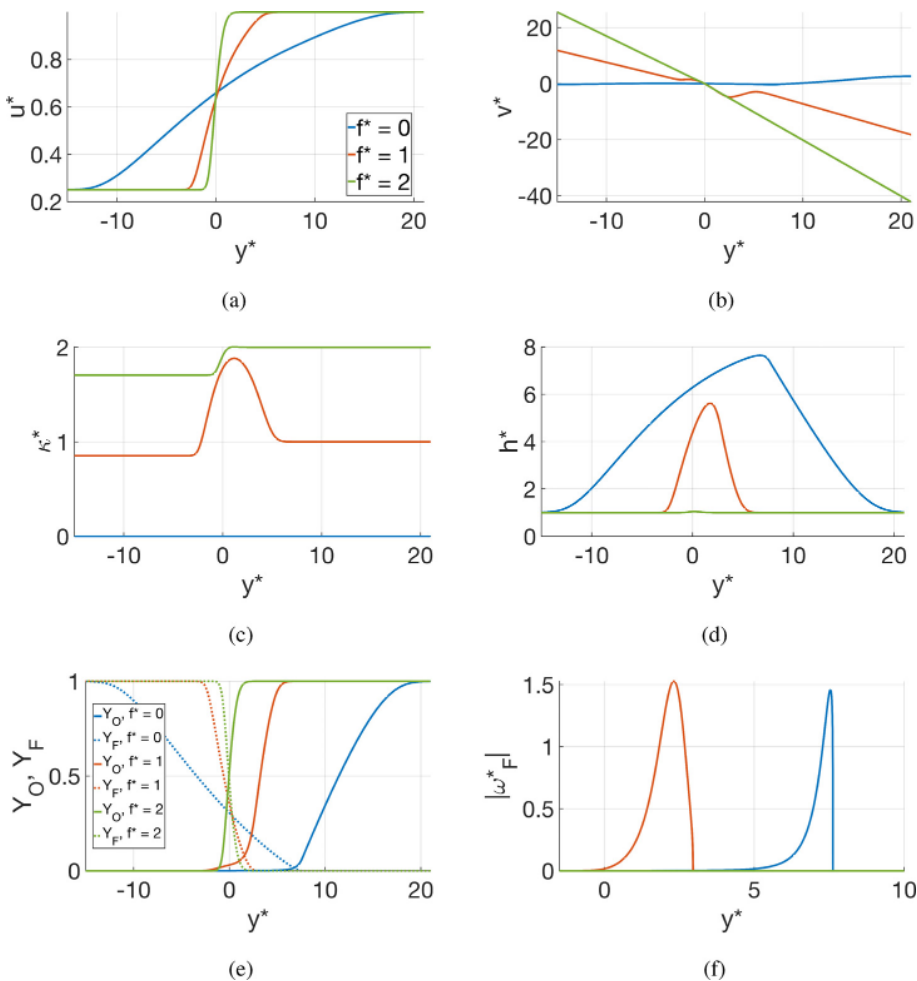

FIG. 10. u^*, v^*, h^*, κ^*, Y_O, Y_F, and $\dot{\omega}_F^*$ at $x^* = 2$ for reactive cases 7a, 6, and 7b. The counterflow strain rate varies from 0 to 2. (a) $u^*(y^*)$, (b) $v^*(y^*)$, (c) $\kappa^*(y^*)$, (d) $h^*(y^*)$, (e) $Y_O(y^*)$, $Y_F(y^*)$, and (f) $|\dot{\omega}_F^*(y^*)|$.

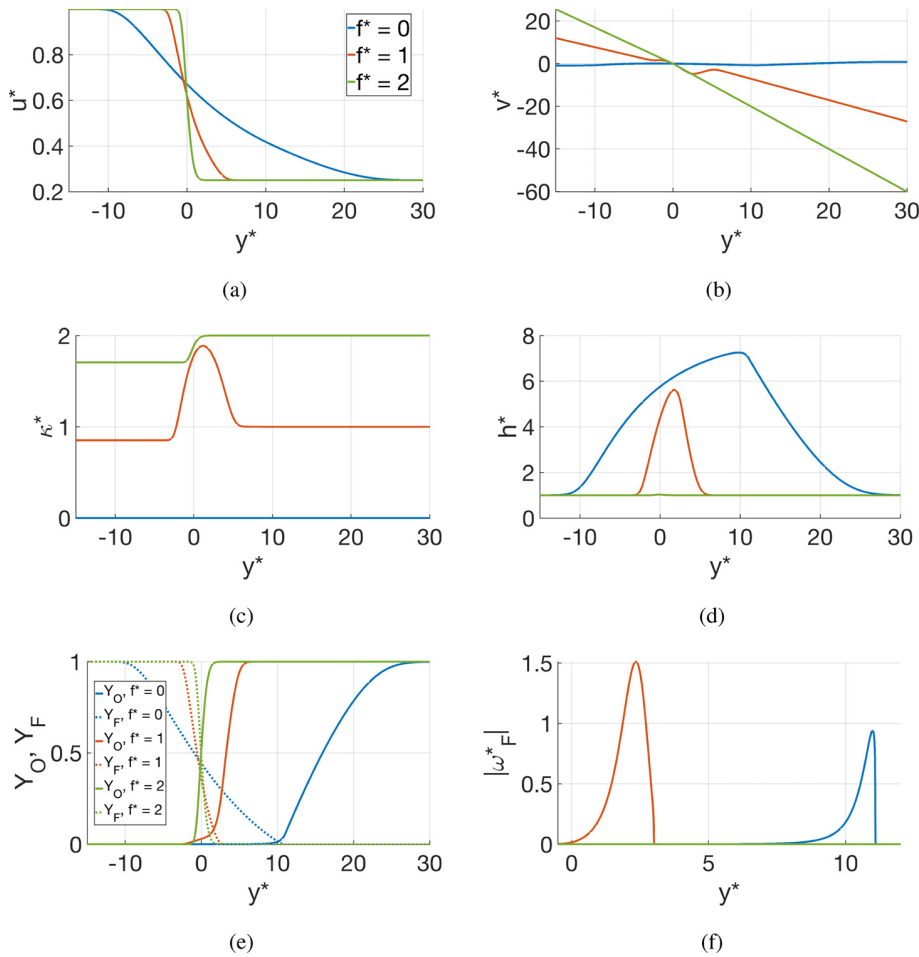FIG. 11. u^*, v^*, h^*, κ^*, Y_O, Y_F, and $\dot{\omega}_F^*$ at $x^* = 2$ for the inverted-velocity reactive cases 11a, 11b, and 11c. The counterflow strain rate varies from 0 to 2. (a) $u^*(y^*)$, (b) $v^*(y^*)$, (c) $\kappa^*(y^*)$, (d) $h^*(y^*)$, (e) $Y_O(y^*)$, $Y_F(y^*)$, and (f) $|\dot{\omega}_F^*(y^*)|$.

substantially downstream, while the reaction zone shifts toward the oxygen-rich stream. The difference of the magnitude indicates that a decreasing burning rate is required with downstream distance. The mixing-layer thickness varies to accommodate the reduced heat flux from the flame.

Figure 10 compares the effects of the two-dimensional flow ($f^* = 0$) to the three-dimensional flow ($f^* \neq 0$) for the reactive case. Figure 10(d) shows that, in the two-dimensional case, the flame grows

to be much wider and hotter than what was initialized upstream. When a counterflow is imposed, the flame is constricted to smaller widths. This compression increases temperature gradients in the y-direction, resulting in faster heat transfer from the reaction zone. A sufficient amount of counterflow ($f^* = 2$) will extinguish the flame, altogether. Residence time is essentially the reciprocal of the strain rate. Although the flame with a counterflow is much smaller and cooler than without, Fig. 10(f) shows that the magnitude of the
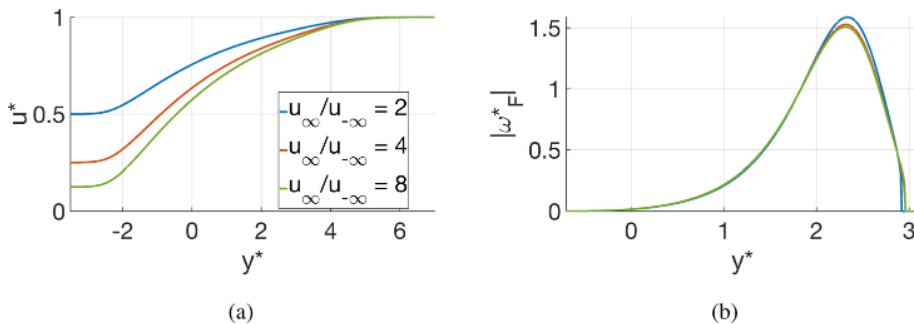

FIG. 12. u^* and $\dot{\omega}_F^*$ at $x^* = 2$ for reactive cases 8a, 6, and 8b. The free-stream velocity ratio varies from 2 to 8. (a) $u^*(y^*)$ and (b) $|\dot{\omega}_F^*(y^*)|$.
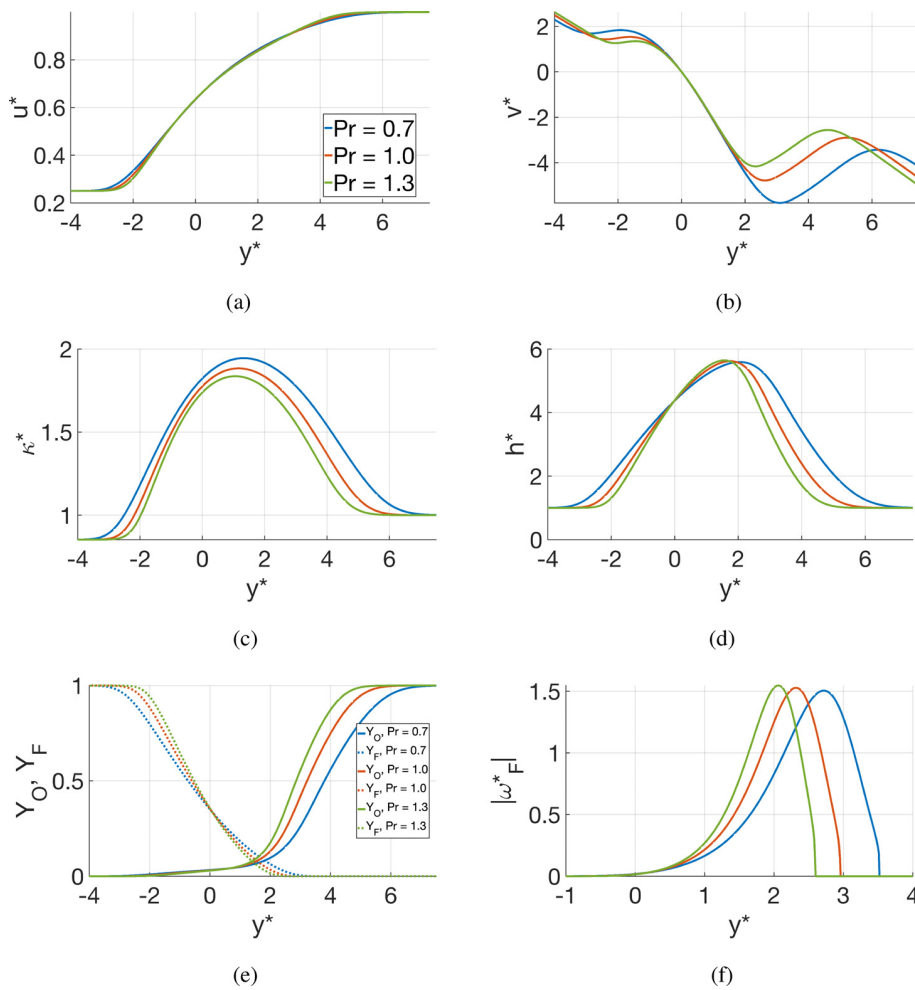
FIG. 13. u^*, v^*, h^*, κ^*, Y_O, Y_F, and $\dot{\omega}_F^*$ at $x^* = 2$ for reactive cases 9a, 6, and 9b. The Prandtl number varies from 0.7 to 1.3. (a) $u^*(y^*)$, (b) $v^*(y^*)$, (c) $\kappa^*(y^*)$, (d) $h^*(y^*)$, (e) $Y_O(y^*)$, $Y_F(y^*)$, and (f) $|\dot{\omega}_F^*(y^*)|$.

reaction rate between the $(f^* = 0)$ and $(f^* = 1)$ cases are very similar. The difference is that the absence of counterflow allows the reaction zone to drift to a greater y-value, toward the oxygen stream. Figure 11(f) shows that the reaction zone will still drift toward the oxygen stream, even if the oxygen stream is slower than the fuel stream.

For this reacting case as well as the prior non-reactive case, the ratio of the free-stream x-component velocities has a very minor effect on the downstream behavior of the scalar quantities when all else is held constant. A slight increase in the burning rate is observed in Fig. 12(f) when the difference in speed between the two streams is lessened. As the velocity of the slower stream is increased, the velocity throughout the layer increases, and less burning occurs near the high-speed stream, as shown in Fig. 12(f). Nevertheless, mass diffusion brings the fuel to a region of larger reaction rate.

Figures 13(c)–13(e) reveal that as Pr increases, the mixing layers for the scalar quantities become thinner for the same reasons discussed in the non-reactive case. In Fig. 13(f), the reaction zone does not drift as far in the positive y-direction with an increased Prandtl number.

Figure 14 compares the reactive cases 6 and 10b to the non-reactive case 10a. The effects of the chemical reaction discussed for case 6 in Fig. 9 are lessened with a decreased Damköhler number in case 10b. When no reaction occurs, the mixing layer for the scalar quantities remains centered at $y^* = 0$ rather than drifting toward the oxygen-rich stream.

D. Multi-flame structures

A premixed fuel-rich flame and premixed fuel-lean flame can co-exist with the primary diffusion flame. This multi-flame case 12 is achieved by changing the ambient mass fraction of the oxidizer in the fast stream from 1 to 11/12 with propane added in the fast stream. The ambient mass fraction of the fuel in the slow stream is decreased from 1 to 2/3 with oxygen added. Figure 15(f) clearly shows multiple flames forming a steady structure far downstream.

In addition to the diffusion flame, a premixed fuel-lean flame is clearly visible in the temperature profiles of Fig. 15(c) as a downward concavity on the positive y-side of the diffusion flame. The premixed fuel-rich flame is not obvious in Fig. 15(c), but Fig. 15(f) shows that a
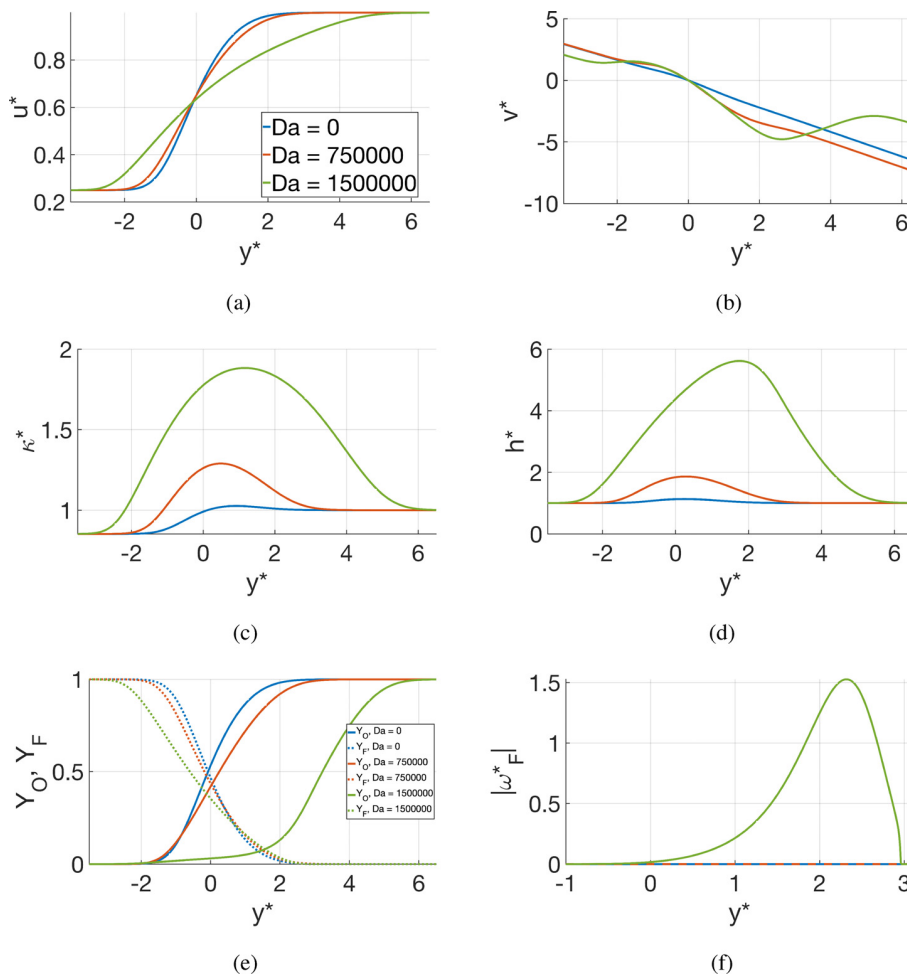
FIG. 14. u^*, v^*, h^*, κ^*, Y_O, Y_F, and $\dot{\omega}_F^*$ at $x^* = 2$ for reactive cases 10a, 6, and 10b. The Damköhler number varies from 0 to 1,500,000. (a) $u^*(y^*)$, (b) $v^*(y^*)$, (c) $\kappa^*(y^*)$, (d) $h^*(y^*)$, (e) $Y_O(y^*)$, $Y_F(y^*)$, and (f) $|\dot{\omega}_F^*(y^*)|$.

fuel-rich premixed reaction is occuring, albeit at a slower rate than the diffusion and fuel-lean premixed flames. Consistent with the previous findings,[29–31] the premixed flames depend on the heat flux from the stronger diffusion flame. At the particular Damköhler number, a premixed flame would not survive independently.

IV. CONCLUDING REMARKS

A fundamental problem for configurations commonly found with turbulent mixing and combustion has been addressed. Specifically, mixing and reaction in a shear layer with vortex stretching has been examined analytically. The downstream asymptotes yield reduced-order behavior which can be helpful in developing flamelet models for turbulent combustion. The laminar treatment is justified for flamelet models because the goal is to represent the behavior of the smallest eddies where the length scale is sufficiently small so that viscous dissipation is strong, and hydrodynamic instabilities with wavelengths comparable to, or shorter than, the smallest eddy size are suppressed.

A constantly imposed counterflow has significant effects on the width of a shear layer downstream. Rather than growing as the square root of downstream distance, as found in two-dimensional shear considerations, the shear-layer width will reach a constant width when a counterflow is imposed with a constant strain rate at all streamwise positions. Far downstream, similarity is achieved as all flow variables, including three velocity components, exhibit one-dimensional behavior varying only with y^* across the shear layer. This asymptotic behavior provides an exact solution to the multicomponent Navier–Stokes equations for both reacting and non-reacting flows. When the counterflow strain rate varies as $1/x^*$, similarity is observed with η for the non-reacting case. In the reacting case, as previously noted,[31] the similarity is only an *ad hoc* approximation because the reacting-layer thickness does not asymptote to a constant value as measured with η.

When chemical reactions are introduced, downstream similarity with y^* is still observed for a constant strain rate imposed along the layer. For sufficient y-direction compression, a flame will extinguish downstream. Here, outward, the spanwise flow decreases the residence time of the combustion reactants, and the thinner mixing layer results in faster
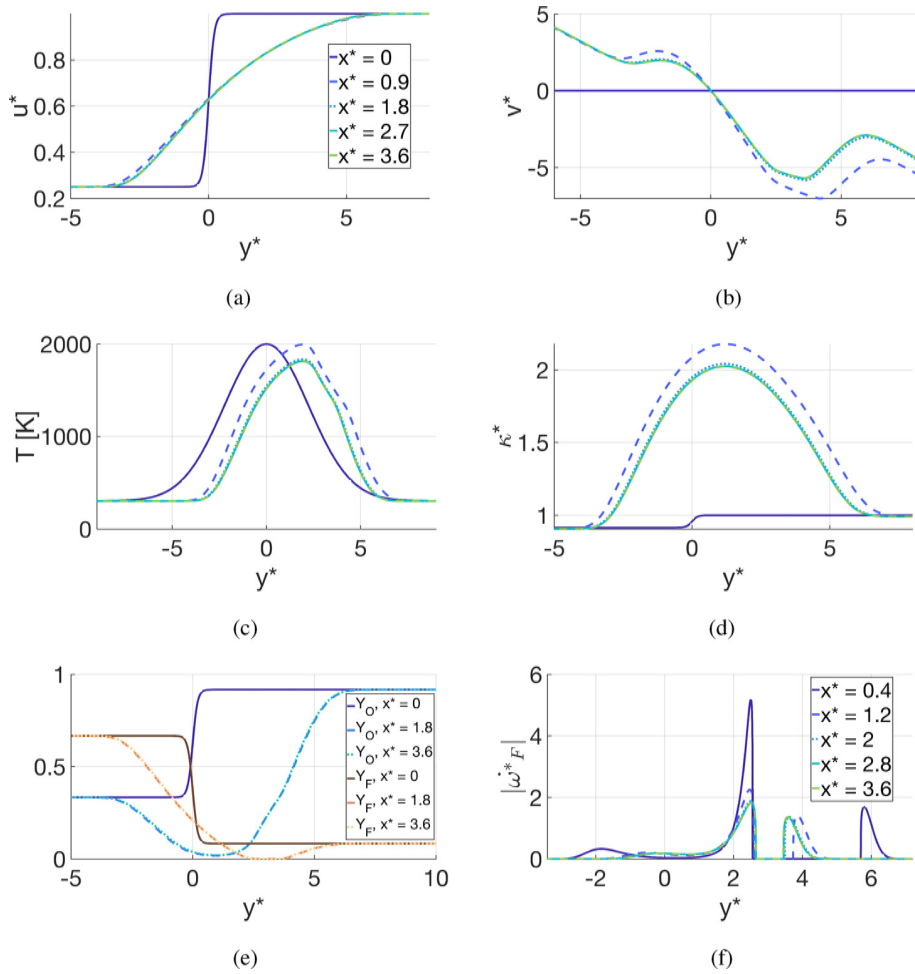
FIG. 15. Results for reactive multi-flame case 12 from $x^* = 0$ to $x^* = 3.6$, where $f^* = 1$. (a) $u^*(y^*)$, (b) $v^*(y^*)$, (c) $T(y^*)$, (d) $\kappa^*(y^*)$, (e) $Y_O(y^*)$, $Y_F(y^*)$, and (f) $|\dot{\omega}_F^*(y^*)|$.
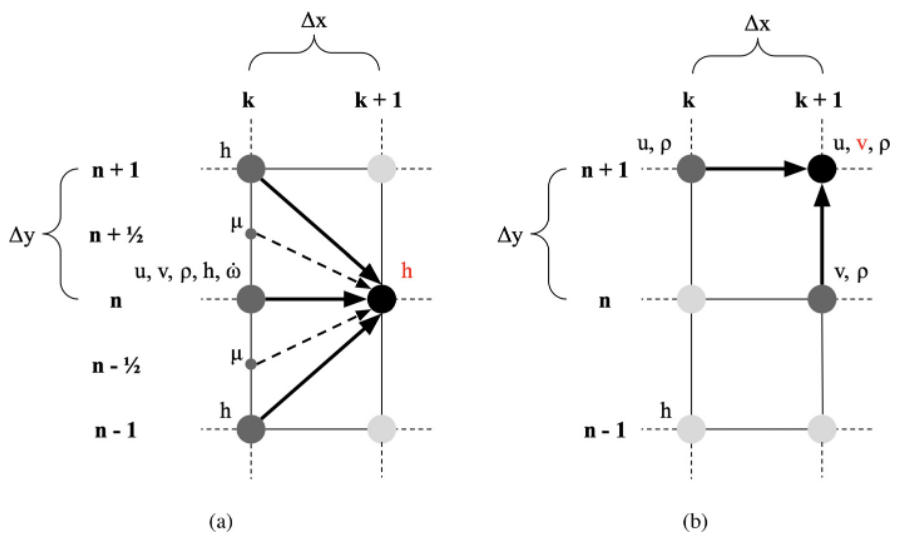

FIG. 16. Subfigure (a) is a visualization of the solution scheme for h after discretizing the energy equation, and (b) is for v after discretizing the continuity equation. In both diagrams, the variable being solved for is colored red at the black solution point. Arrows travel toward solution points from their dependee grid points is colored dark gray.

heat transfer. Likewise, there is a range of imposed strain rate where a flame does not extinguish and maintains its form similarly downstream. Furthermore, multi-flame structures can become similar downstream, depending only on the y-position.

The simple computational method is inexpensive for the boundary-layer calculations here, and mesh-size independence is demonstrated. The fact that the calculations produce the similar solutions as asymptotes in different cases also justifies strong confidence.

Future studies might use more rigorous multi-step chemical-reaction models. Gases might be modeled as real for a high-pressure domain. Rather than selecting the linear behavior of the flow in the z-direction, a three-dimensional numerical solution might be developed, testing for higher-order effects for the spanwise flow.

The asymptotic downstream quasi-one-dimensional behavior with three meaningful velocity components offers interesting possibilities for future computational and experimental research. This fully developed downstream behavior retains the major features of the flow: shear and vorticity, mixing, applied strain and counterflow, and three velocity components. Researchers often seek to examine the new concepts in configurations that include key physics but reduce the dimensionality of the problem. Here, we have qualitative similarity to the fully developed Poiseuille channel flow where only one-dimension is needed to describe the variation in the flow field. However, in this case, it retains three meaningful velocity components and is better suited for studies where heat and mass transport are important.

AUTHOR DECLARATIONS

Conflict of Interest

The authors have no conflicts to disclose.

Author Contributions

Jonathan Louis Palafoutas: Conceptualization (equal); Data curation (equal); Formal analysis (equal); Investigation (equal); Methodology (equal); Resources (equal); Software (equal); Validation (equal); Visualization (equal); Writing – original draft (equal); Writing – review & editing (equal). **William A. Sirignano:** Conceptualization (equal); Formal analysis (equal); Investigation (equal); Methodology (equal); Resources (equal); Software (equal); Validation (equal); Writing – original draft (equal); Writing – review & editing (equal).

DATA AVAILABILITY

The data that support the findings of this study are available from the corresponding author upon reasonable request.

APPENDIX: DISCRETIZED EQUATIONS FOR SOLUTION SCHEME

Following the notation $h_n^k \approx h(x, y)$, $h_n^{k+1} \approx h(x + \Delta x, y)$, and $h_{n+1}^k \approx h(x, y + \Delta y)$, we discretize the energy equation to solve for h at the $k + 1$th position in x, given data from the kth position as follows:

$$
h_n^{k+1} = h_n^k + \frac{\Delta x}{\rho_n^k u_n^k} \left[\frac{1}{Pr} \frac{1}{\Delta y^2} \left(\mu_{n+\frac{1}{2}}^k h_{n+1}^k - \mu_{n+\frac{1}{2}}^k h_n^k - \mu_{n-\frac{1}{2}}^k h_n^k + \mu_{n-\frac{1}{2}}^k h_{n-1}^k \right) \right.
$$
$$
\left. - \rho_n^k v_n^k \frac{h_{n+1}^k - h_{n-1}^k}{2\Delta y} - Q \rho_n^k \dot{\omega}_{F,n}^k \right], \tag{A1}
$$

where the meaning of $n \pm \frac{1}{2}$ is explained in Eqs. (22) and (23). Thus, the "downstream march" is defined. Figure 16(a) illustrates the dependency of the solution at a grid point on upstream points. The momentum and species continuity equations are discretized mutatis mutandis as they follow the same form as the energy equation.

The continuity equation requires a different scheme because it contains no x-derivative of v, meaning a downstream march cannot be implemented. We take advantage of the y-derivative of v and devise a transverse march in the y-direction

$$
v_{n+1}^{k+1} = v_n^{k+1} - \frac{\Delta y}{\rho_{n+1}^{k+1}} \left[u_{n+1}^{k+1} \frac{\rho_{n+1}^{k+1} - \rho_{n+1}^k}{\Delta x} + \rho_{n+1}^{k+1} \frac{u_{n+1}^{k+1} - u_{n+1}^k}{\Delta x} \right.
$$
$$
\left. + v_n^{k+1} \frac{\rho_{n+1}^{k+1} - \rho_n^{k+1}}{\Delta y} + \rho_{n+1}^{k+1} \kappa_{n+1}^{k+1} \right] \tag{A2}
$$

using the same notation as Eq. (A1). This march occurs at the $k + 1$th position in x and solves for v at the $n + 1$th position in y, as depicted in Fig. 16(b). Recall that the boundary condition for v lies at $y = 0$, so the scheme must be implemented twice: once traveling in the positive y-direction and once traveling in the negative y-direction with Δy becoming $-\Delta y$ and $n + 1$ becoming $n - 1$. Furthermore, this scheme must be executed after the schemes for the x-momentum and energy equations, as the solution depends on knowing u and $\rho(h)$ at the $k + 1$th position in x.

Note that for Eqs. (A1) and (A2), the superscript notation for non-dimensional variables is omitted in favor of legibility. Nevertheless, these equations hold if the values are normalized as in Eqs. (10)–(15).

REFERENCES

[1] W. A. Sirignano, "Three-dimensional, rotational flamelet closure model with two-way coupling," J. Fluid Mech. **945**, A21 (2022).

[2] W. A. Sirignano, "Inward swirling flamelet model," Combust. Theory Modell. **26**, 1014 (2022).

[3] W. A. Sirignano, "Stretched vortex layer flamelet," Combust. Flame **244**, 112276 (2022).

[4] R. Betchov, "An inequality concerning the production of vorticity in isotropic turbulence," J. Fluid Mech. **1**, 497–504 (1956).

[5] W. Ashurst, A. R. Kerstein, R. M. Kerr, and C. H. Gibson, "Alignment of vorticity and scalar gradient with strain rate in simulated Navier-Stokes turbulence," Phys. Fluids **30**, 2343–2352 (1987).

[6] K. K. Nomura and S. E. Elghobashi, "Mixing characteristics of an inhomogeneous scalar in isotropic and homogeneous sheared turbulence," Phys. Fluids A **4**, 606–625 (1992).

[7] E. Dresselhaus and M. Tabor, "On the viscous core of a line vortex," J. Fluid Mech. **236**, 415–444 (1992).

[8] R. M. Kerr, "Histograms of helicity and strain in numerical turbulence," Phys. Rev. Lett. **59**, 783–786 (1987).

[9] K. K. Nomura and S. E. Elghobashi, "The structure of inhomogeneous turbulence scalar in variable density nonpremixed flames," Theor. Comput. Fluid Dyn. **5**, 153–175 (1993).

[10] O. N. Boratav, S. E. Elghobashi, and R. Zhong, "On the alignment of the a-strain and vorticity in turbulent nonpremixed flames," Phys. Fluids **8**, 2251–2253 (1996).

[11] O. N. Boratav, S. E. Elghobashi, and R. Zhong, "On the alignment of strain, vorticity and scalar gradient in turbulent, buoyant, nonpremixed flames," Phys. Fluids **10**, 2260–2267 (1998).

[12] J. C. Neu, "The dynamics of stretched vortices," J. Fluid Mech. **143**, 253–276 (1984).

[13]G. Corcos and F. Sherman, "The mixing layer: Deterministic models of a turbulent flow. part 1. introduction and the two-dimensional flow," J. Fluid Mech. **139**, 29–65 (1984).

[14]G. Corcos and S. J. Lin, "The mixing layer: Deterministic models of a turbulent flow. Part 2. The origin of the three-dimensional motion," J. Fluid Mech. **139**, 67–95 (1984).

[15]S. J. Lin and G. Corcos, "The mixing layer: Deterministic models of a turbulent flow. Part 3. The effect of plane strain on the dynamics of streamwise vortices," J. Fluid Mech. **141**, 139–178 (1984).

[16]K. A. Buch and W. J. A. Dahm, "Experimental study of fine-scale structure of conserved scalar mixing in turbulent shear flows. Part 2. Sc $\approx$ 1," J. Fluid Mech. **364**, 1–29 (1998).

[17]J. M. Burgers, "A mathematical model illustrating the theory of turbulence," Adv. Appl. Mech. **1**, 171–199 (1948).

[18]N. Rott, "On the viscous core of a line vortex," Z. Angew. Math. Phys. **9**, 543–553 (1958).

[19]J. M. Burgers, *Unpublished Lectures on Turbulence* (California Institute of Technology, 1951).

[20]G. K. Batchelor, *An Introduction to Fluid Dynamics* (Cambridge University Press, 1967), p. 273.

[21]P. G. Saffman, *Vortex Dynamics* (Cambridge University Press, 1992).

[22]F. A. Williams, *Combustion Theory*, 2nd ed. (CRC Press, 1985).

[23]A. Linán, "The asymptotic structure of counterflow diffusion flames for large activation energies," Acta Astronaut. **1**, 1007–1039 (1974).

[24]N. Peters, *Turbulent Combustion*, 1st ed. (Cambridge University Press, 2000).

[25]F. Williams, "Progress in knowledge of flamelet structure and extinction," Prog. Energy Combust. Sci. **26**, 657–682 (2000).

[26]C. D. Pierce and P. Moin, "Progress-variable approach for large-eddy simulation of non-premixed turbulent combustion," J. Fluid Mech. **504**, 73–97 (2004).

[27]P. Rajamanickam, W. Coenen, A. L. Sánchez, and F. A. Williams, "Influences of stoichiometry on steadily propagating triple flames in counterflows," Proc. Combust. Inst. **37**, 1971–1977 (2019).

[28]W. A. Sirignano, "Counterflow and wall stagnation flow with three-dimensional strain," Phys. Fluids **31**, 053605 (2019).

[29]W. A. Sirignano, "Combustion with multiple flames under high strain rates," Combust. Sci. Technol. **193**, 1173–1202 (2021).

[30]W. A. Sirignano, "Diffusion-controlled premixed flames," Combust. Theory Modell. **25**, 1019–1038 (2021).

[31]W. A. Sirignano, "Mixing and combustion in a laminar shear layer with imposed counterflow," J. Fluid Mech. **908**, A35 (2021).

[32]L. Crocco, "Transmission of heat from a flat plate to a fluid flowing at a high velocity," Technical Memorandum No. 690 (National Advisory Committee for Aeronautics, 1932).

[33]L. Howarth, "Concerning the effect of compressibility on laminar boundary layers and their separation," Proc. R. Soc. London, Ser. A **194**, 16–42 (1948).

[34]C. Illingworth, "Steady flow in the laminar boundary layer of a gas," Proc. R. Soc. London, Ser. A **199**, 533–558 (1949).

[35]K. Stewartson, "Correlated incompressible and compressible boundary layers," Proc. R. Soc. London, Ser. A **200**, 84–100 (1949).

[36]R. Bilger, "The structure of diffusion flames," Combust. Sci. Technol. **13**, 155–170 (1976).

[37]A. Linán and F. Williams, "Ignition in an unsteady mixing layer subject to strain and variable pressure," Combust. Flame **95**, 31–46 (1993).

[38]C. K. Westbrook and F. L. Dryer, "Chemical kinetic modeling of hydrocarbon combustion," Prog. Energy Combust. Sci. **10**, 1–57 (1984).

[39]T. H. Chung, M. Ajlan, L. L. Lee, and K. E. Starling, "Generalized multiparameter correlation for nonpolar and polar fluid transport properties," Ind. Eng. Chem. Res. **27**, 671–679 (1988).

[40]J. H. Ferziger and M. Perić, *Computational Methods for Fluid Dynamics* (Springer-Verlag, Berlin, Heidelberg, 1996), pp. 136–138.